# Riemann-Finsler Multi-valued Geodesic Tractography for HARDI

**Neda Sepasian, Jan H.M. ten Thije Boonkkamp, Luc M.J. Florack,
Bart M. Ter Haar Romeny, and Anna Vilanova**

**Abstract** We introduce a geodesic based tractography method for High Angular Resolution Diffusion Imaging (HARDI). The concepts used are similar to the ones in geodesic based tractography for Diffusion Tensor Imaging (DTI). In DTI, the inverse of the second-order diffusion tensor is used to define the manifold where the geodesics are traced. HARDI models have been developed to resolve complex fiber populations within a voxel, and higher order tensors (HOT) are possible representations for HARDI data. In our framework, we apply Finsler geometry, which extends Riemannian geometry to a directionally dependent metric. A Finsler metric is defined in terms of HARDI higher order tensors. Furthermore, the Euler-Lagrange geodesic equations are derived based on the Finsler geometry. In contrast to other geodesic based tractography algorithms, the multi-valued numerical solution of the geodesic equations can be obtained. This gives the possibility to capture all geodesics arriving at a single voxel instead of only computing the shortest one. Results are analyzed to show the potential and characteristics of our algorithm.

---

N. Sepasian • L.M.J. Florack
Department of Biomedical Engineering, Mathematics and Computer Science,
Eindhoven University of Technology, PO Box 513, 5600 MB Eindhoven, The Netherlands
e-mail: nsepasian@gmail.com; L.M.J.Florack@tue.nl

J.H.M. ten Thije Boonkkamp
Mathematics and Computer Science, Eindhoven University of Technology, PO Box 513,
5600 MB Eindhoven, The Netherlands
e-mail: J.H.M.tenThijeBoonkkamp@tue.nl

B.M. Ter Haar Romeny
Department of Biomedical Engineering, Eindhoven University of Technology, PO Box 513,
5600 MB Eindhoven, The Netherlands
e-mail: B.M.terHaarRomeny@tue.nl

A. Vilanova (✉)
Faculty Electrical Engineering, Mathematics and Computer Science, Computer Graphics
and Visualization, Delft University of Technology, Delft, The Netherlands
e-mail: A.Vilanova@tudelft.nl

C.-F. Westin et al. (eds.), *Visualization and Processing of Tensors and Higher Order Descriptors for Multi-Valued Data*, Mathematics and Visualization,
DOI 10.1007/978-3-642-54301-2_9, © Springer-Verlag Berlin Heidelberg 2014

# 1 Introduction

Diffusion-Weighted Magnetic Resonance Imaging(DW-MRI) measures water diffusion characteristics in tissue for a given direction. The diffusion profile in a specific location can be obtained by combining the DW-MRI measurements in different directions. The diffusion profile gives information about the underlying fibrous structure, e.g., in human brain white matter, based on the assumption that water molecules are moving less freely perpendicular to the fibrous structure than along the fiber tracts. Techniques to reconstruct fiber tracts based on the diffusion profiles are known as tractography or fiber tracking methods.

From DW-MRI measurements often a positive definite second-order tensor is defined, referred to as diffusion tensor imaging (DTI) [4]. Despite the simplicity of the model, this technique is shown to be promising to reveal the structure of brain white matter. However, DTI assumes that each voxel contains fibers with only one orientation, and it is known that in white matter often multiple fiber orientations occur [2]. High Angular Resolution Diffusion Imaging (HARDI) and its modeling techniques have been developed to overcome the limitations of the DTI model [12, 19, 27, 29–31].

The models applied to HARDI data result in a function on the unit sphere that gives information about the diffusion profile within the voxel. This function on the unit sphere is obtained by different assumptions and models of the diffusion and acquisition process. In general, the diffusion profiles are assumed to have local maxima in the orientations of the underlying fiber tracts. One of the most popular models is to use the Orientation Distribution Function (ODF) [12, 28, 30]. An extensive description of the different HARDI models is considered outside the scope of this chapter. However, it should be noticed that any function on the unit sphere, and therefore any HARDI model, can be represented by Higher Order Tensors (HOT).

Numerous tractography algorithms have been introduced to reconstruct the fibrous structure from DTI and HARDI data. In the most commonly used tractography algorithms, i.e., streamline based methods, the fibers are estimated by using a number of directions (i.e., the principal direction of the diffusion tensor [4] or the local maxima in the HARDI models [15]). These methods are based on local characteristics and therefore sensitive to noise. A possible solution to resolve these limitations of classic tractography, is to apply global approaches such as geodesic based algorithms [7, 14, 16]. These techniques are based on the assumption that fibers follow the most efficient diffusion propagation paths. A Riemannian manifold is defined using as metric the inverse of the diffusion tensor. Paths in this manifold are shorter if the diffusion is stronger along that path. Therefore, geodesics (i.e., shortest paths) in this manifold follow the most efficient diffusion paths. The global approaches are considerably more computationally expansive than the streamline based methods.

Sepasian et al. [24] presented a ray-tracing algorithm for computing geodesics in anisotropic domains. Common geodesic based methods obtain the viscosity solution based on the Hamilton-Jacobi equation and by solving it numerically using different numerical schemes, e.g., fast-sweeping. These methods are robust and mathematically elegant. However, the viscosity solution provides only one geodesic between two given points in the domain. In contrast, the approach of Sepasian et al. [24] can capture multi-valued geodesics connecting two given points by considering the geodesics as function of position and direction. Moreover, it is based on the Euler-Lagrange (EL) equations, and therefore local changes in the geodesic can be taken into account. However, this method remains limited to Riemannian manifolds and, therefore, to DTI models.

Campbell [8] proposed a front evolution approach based on HARDI. Pichon et al. [22] introduced a variational cost function depending on all directions on the unit sphere. This directional information is obtained using HARDI. Péchaud et al. [21] presented an algorithm for the calculation of shortest paths on a manifold defined by ODFs. The metric for each position is defined as the orientation distribution function and the geodesics locally follow the paths going through areas of high diffusion.

The methods mentioned above belong to the class of deterministic tractography methods, i.e., given the same input these methods will always give the same result. In the generic case, geodesic-based methods will find a finite number of geodesic paths given two points in the domain. Probabilistic tractography constitutes another class of methods where the variation of the pathways due to model assumptions and/or noise is considered. A probability distribution is built, and based on this distribution, a random process generates many paths originating from one initial position [10, 20]. HARDI tractography techniques are often probabilistic [5, 13].

In this chapter, we propose an extension to HARDI data of the method introduced by Sepasian et al. [24]. Riemannian metric depends on the position in space, and it has no directional dependency. A Riemannian framework is well suited for DTI data, but not for HARDI data. Finsler geometry is the natural extension of the Riemannian geometry to directional dependent metrics. In a Finsler metric, for each position and direction we might have a different metric tensor. Therefore, to extend the work of Sepasian et al. [24] to HARDI data, we need to extend it to Finsler geometry. You can find further explanation on the Riemannian-Finsler geometry in the chapter *Riemann-Finsler Geometry for Diffusion Weighted Magnetic Resonance Imaging*. In comparison to previous work, e.g., Péchaud et al. [21], our technique is based on minimizing the length using the geodesic equations in Finsler geometry instead of a general cost function. Melonakos et al. [17] presented a tractography method for Finsler geometry within their active contours segmentation framework. Their method is based on DTI data and the Finsler metric is used to reduce signal to noise ratio. Furthermore, we uniquely compute the multi-valued solution of the geodesic equations between two points in the domain instead of the single-valued viscosity solution.

The chapter is organized as follows. In Sect. 2 we introduce Finsler geometry which extends Riemannian geometry to directionally dependent metrics. We introduce the Euler-Lagrange form of the geodesic equations in the Finsler geometry in Sect. 3. Next, in Sect. 4, we describe the numerical model necessary for the implementation of the presented ray-tracing algorithm. Finally, preliminary results are presented in Sect. 5.

## 2 Finsler Metric

In this chapter, we consider the generalization to higher order tensors as an extension of the second order tensors. Higher order tensors allow the representation of multiple fiber orientations. For simplicity, we present the theory for fourth order tensors, although, its extension to higher orders can be trivially deduced. $P_4(\mathbf{x}, \mathbf{y})$ is a function on the unit sphere that represent the diffusion profile obtained by one of the HARDI modeling techniques. At this point, the theory is presented in a general form such that $P_4(\mathbf{x}, \mathbf{y})$ can be the diffusion profile resulting from diverse HARDI modeling techniques, as long as the diffusion flux increases with increasing values of $P_4(\mathbf{x}, \mathbf{y})$.

We fit the fourth order tensor coefficients $\mathbf{D} = \mathbf{D}(\mathbf{x})$ to the function $P_4(\mathbf{x}, \mathbf{y})$ by using the sampled data on the unit sphere [12], i.e.,

$$P_4(\mathbf{x}, \mathbf{y}) = D_{\alpha_1\alpha_2\alpha_3\alpha_4}(\mathbf{x}) y^{\alpha_1} y^{\alpha_2} y^{\alpha_3} y^{\alpha_4}, \tag{1}$$

with $\alpha_i = 1, 2, 3$, $i = 1, 2, 3, 4$, $\mathbf{x}$ contains the spatial coordinates and $\mathbf{y} = (y^{\alpha_i}) = (\sin\theta\cos\phi, \sin\theta\sin\phi, \cos\theta)$ is the directional vector with $\phi \in [0, 2\pi)$ and $\theta \in [0, \pi]$. Here, the coefficients $D_{\alpha_1\alpha_2\alpha_3\alpha_4}(\mathbf{x})$ are the elements of $\mathbf{D}$. Note that in all the formulas the Einstein summation convention is used, i.e., we sum over repeated indices, one in a superscript and one in subscript position. The tensor $\mathbf{D}$ satisfies the symmetry property,

$$D_{\alpha_1\alpha_2\alpha_3\alpha_4} = D_{\sigma(\alpha_1)\sigma(\alpha_2)\sigma(\alpha_3)\sigma(\alpha_4)}, \tag{2}$$

for any permutation $\sigma$. Therefore we can reduce the number of components from 81 to 15.

Similar to the DTI Riemannian framework, we use the heuristic that a high probability of finding a fiber in direction $\mathbf{y}$ corresponds to a larger diffusivity represented in $P_4(\mathbf{x}, \mathbf{y})$, and a shorter travel time for the diffusing particle. Therefore, the metric should give the shortest distance in the direction where diffusion is largest. In DTI this is achieved by introducing the metric as the inverse of the diffusion tensor. Consequently, the largest eigenvalue of the diffusion tensor becomes the smallest one for the metric. In contrast, in HARDI we deal with more complex diffusion profiles. We need to extend the framework to a Finsler geometry where the metric is function of position and direction. Furthermore, we need to find a suitable framework for inverting the HOT. A proper inversion should preserve certain properties including the average value of the function and the angle between two directions [6]. Astola et al. [3] suggest to use spherical inversion for the HARDI diffusion profile. Figure 1 illustrates the spherical inversion of a point on a surface $M$ with coordinates $\mathbf{x}_M$. The inverse of a point $M$ with respect to a reference sphere centered at the origin $O$ with radius $r = a$ is the point $M'$ such that $|\mathbf{x}_M| \times |\mathbf{x}_{M'}| = a^2$ where $\mathbf{x} = r\mathbf{e}_r$ is the position vector and $\mathbf{e}_r$ is the radial unit vector in spherical coordinates. The points $M$ and $M'$ are on the same ray through $O$. Figure 1 shows that the inversion maps points that were outside the

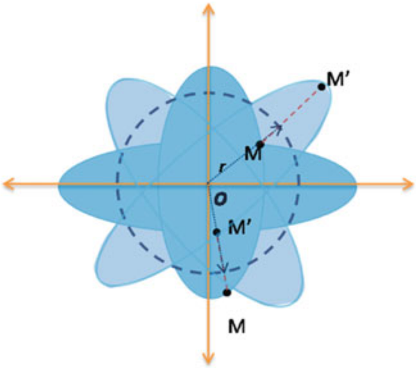

**Fig. 1** An illustration of spherical inversion in two dimensions. $M'$ is the inverse of $M$ with respect to the circle

sphere to points that are inside the sphere, and vice versa. For example, for the case when $M$ is outside the reference sphere, $|\mathbf{x}_M| > a$ which gives

$$|\mathbf{x}_{M'}| = \frac{a^2}{|\mathbf{x}_M|} < a.$$

In analogy with the spherical inversion, we define $\tilde{P}_4(\mathbf{x}, \mathbf{y})$, which is the inverse of $P_4(\mathbf{x}, \mathbf{y})$, as follows

$$\tilde{P}_4(\mathbf{x}, \mathbf{y}) = \frac{\overline{P_4}(\mathbf{x})}{P_4(\mathbf{x}, \mathbf{y})} = \tilde{D}_{\alpha_1\alpha_2\alpha_3\alpha_4}(\mathbf{x}) y^{\alpha_1} y^{\alpha_2} y^{\alpha_3} y^{\alpha_4}, \tag{3}$$

where $\tilde{\mathbf{D}}$ is the HOT that fits $\tilde{P}_4(\mathbf{x}, \mathbf{y})$ and $\overline{P_4}(\mathbf{x})$ is the average of the HOT over the unit sphere, i.e.,

$$\overline{P_4}(\mathbf{x}) = \int_{|\mathbf{y}|=1} P_4(\mathbf{x}, \mathbf{y}) \mathrm{d}\mathbf{y}.$$

Astola et al. [3] propose the following Finsler norm for the fourth order tensors

$$F(\mathbf{x}, \mathbf{y}) = (\tilde{P}_4(\mathbf{x}, \mathbf{y}))^{1/4}. \tag{4}$$

It can be shown that the Finsler metric is given by the bilinear form $F = F(\mathbf{x}, \mathbf{y})$ as follows

$$g_{\alpha\beta}(\mathbf{x}, \mathbf{y}) = \frac{1}{2} \frac{\partial^2 F^2}{\partial y^\alpha \partial y^\beta} \tag{5}$$

where $\alpha$ and $\beta$ are used to index the components of the tensor $g$.

In the following, we illustrate that the Riemannian metric is a special case of the Finsler metric. If $F^2(\mathbf{x}, \mathbf{y}) = g_{\alpha\beta}(\mathbf{x}) y^\alpha y^\beta$, i.e., $g_{\alpha\beta}$ only depends on $\mathbf{x}$, then

**Fig. 2** Illustration of the directional dependency of tensors $g_{\alpha\beta}(\mathbf{x},\mathbf{y})$. The $\tilde{P}_4(\mathbf{x},\mathbf{y})$ profile is shown as a surface in all images. The *arrows* indicate specific directions $\mathbf{y}$, and the ellipsoids represent the tensors $g_{\alpha\beta}(\mathbf{x},\mathbf{y})$ calculated from $\tilde{P}_4(\mathbf{x},\mathbf{y})$ by fixing the direction $\mathbf{y}$ for each image

$$g_{\alpha\beta}(\mathbf{x},\mathbf{y}) = \frac{1}{2}\frac{\partial^2}{\partial y_\alpha \partial y_\beta}\left(g_{\alpha\beta}(\mathbf{x}) y^\alpha y^\beta\right) = g_{\alpha\beta}(\mathbf{x}), \tag{6}$$

known as the Riemannian metric. In contrast, Finsler metric does not only depend on the location $\mathbf{x}$ but also on the direction $\mathbf{y}$.

The necessary conditions of differentiability, homogeneity and strong convexity for (4) have been studied in Astola et al. [3] and the strong convexity criterion only holds if the second-order tensor $D_{\alpha_1\alpha_2\alpha_3\alpha_4} y^{\alpha_1} y^{\alpha_2}$ is positive definite for every $\mathbf{y}$. In practice this condition turns out to be satisfied.

Substituting (4) in the bilinear form (5), we can show that the Finsler metric tensor reads

$$\begin{aligned} g_{\alpha\beta}(\mathbf{x},\mathbf{y}) &= \frac{1}{2}\frac{\partial^2}{\partial y^\alpha y^\beta} F^2(\mathbf{x},\mathbf{y}) \\ &= -2\tilde{P}_4(\mathbf{x},\mathbf{y})^{-3/2}\left(\tilde{D}_{\alpha\alpha_1\alpha_2\alpha_3} y^{\alpha_1} y^{\alpha_2} y^{\alpha_3}\right)\left(\tilde{D}_{\beta\beta_1\beta_2\beta_3} y^{\beta_1} y^{\beta_2} y^{\beta_3}\right) \\ &+ 3\tilde{P}_4(\mathbf{x},\mathbf{y})^{-1/2}\tilde{D}_{\alpha\beta\alpha_1\alpha_2} y^{\alpha_1} y^{\alpha_2}. \end{aligned} \tag{7}$$

This means that at each position $\mathbf{x}$ and for each choice of $\mathbf{y}$, we can obtain the corresponding local metric. Figure 2 illustrates the directional dependence of the Finsler metric for a given $\tilde{P}_4(\mathbf{x},\mathbf{y})$ profile. Three different tensors $g_{\alpha\beta}(\mathbf{x},\mathbf{y})$ are obtained for the same profile, i.e., position $\mathbf{x}$, by changing $\mathbf{y}$. The metric tensors are necessary to be able to compute geodesics in the Finsler geometry framework.

## 3 Geodesic Equations for the Finsler Metric

Analogous to the Riemannian case, in Finsler metric geodesics are the curves that minimize the length between fixed endpoints. We consider a bounded curve $\mathscr{C}$ with parametrization $\mathbf{x} = \boldsymbol{\chi}(t)$, $a \leq t \leq b$, where $t$ denotes the arc-length. The length of $\mathscr{C}$ is given by,

$$J[\chi] = \int_a^b F(\chi(t), \dot{\chi}(t))\mathrm{d}t \tag{8}$$

where $\dot{\chi}(t) = \frac{\mathrm{d}\chi(t)}{\mathrm{d}t}$. It can be shown that the necessary condition to minimize the length functional (8) is the set of Euler-Lagrange equations [18, 23, 26],

$$\frac{\mathrm{d}}{\mathrm{d}t}\left(\frac{\partial F}{\partial y^\alpha}\right) - \frac{\partial F}{\partial x^\alpha} = 0, \tag{9}$$

where $y^\alpha = \dot{x}^\alpha$. We will derive the geodesic equations from Eq. (9). First, straightforward application of the chain rule gives

$$\frac{\mathrm{d}}{\mathrm{d}t}\left(\frac{\partial F^2}{\partial y^\alpha}\right) - \frac{\partial F^2}{\partial x^\alpha} = \frac{1}{F}\frac{\mathrm{d}F}{\mathrm{d}t}\frac{\partial F^2}{\partial y^\alpha}. \tag{10}$$

Using that $\frac{\mathrm{d}F}{\mathrm{d}t} = 0$ (arclength parametrization), the above equation simplifies to,

$$\frac{\mathrm{d}}{\mathrm{d}t}\left(\frac{\partial F^2}{\partial y^\alpha}\right) - \frac{\partial F^2}{\partial x^\alpha} = 0. \tag{11}$$

Once more applying the chain rule and substitution of (5) gives

$$2g_{\alpha\beta}\ddot{x}^\beta + \frac{\partial^2 F^2}{\partial y^\alpha \partial x^\beta} y^\beta - \frac{\partial F^2}{\partial x^\alpha} = 0. \tag{12}$$

Multiplying Eq. (12) with the inverse $g^{\gamma\alpha}$ gives

$$\ddot{x}^\alpha + 2G^\alpha(\mathbf{x}, \dot{\mathbf{x}}) = 0, \tag{13}$$

where $G^\alpha$ are the so-called geodesic coefficients defined by

$$G^\alpha(\mathbf{x}, \mathbf{y}) = \frac{1}{4} g^{\alpha\beta}(\mathbf{x}, \mathbf{y})\left(\frac{\partial^2 F^2(\mathbf{x}, \mathbf{y})}{\partial y^\beta \partial x^\gamma} y^\gamma - \frac{\partial F^2(\mathbf{x}, \mathbf{y})}{\partial x^\beta}\right). \tag{14}$$

It is often useful from a computational point of view to write the geodesic Eq. (13) in an alternative form. To this purpose we introduce the Christoffel symbols (of second kind) $\Gamma^\alpha_{\beta\gamma}$ defined as

$$\Gamma^\alpha_{\beta\gamma}(\mathbf{x}, \mathbf{y}) = \frac{1}{2} g^{\alpha\kappa}(\mathbf{x}, \mathbf{y})\left(\frac{\partial g_{\beta\kappa}}{\partial x^\gamma} + \frac{\partial g_{\gamma\kappa}}{\partial x^\beta} - \frac{\partial g_{\beta\gamma}}{\partial x^\kappa}\right). \tag{15}$$

Note that compared to the Riemannian case, $\Gamma^\alpha_{\beta\gamma}$ are functions of both space and orientation. To reformulate the geodesic equations, we essentially rewrite $G^\alpha$

in terms of the formal Christoffel symbols [9]. Indeed, we have the following proposition:

**Proposition 1.** *The geodesic coefficients $G^\alpha$ defined in (14), are related to the Christoffel symbols $\Gamma^\alpha_{\beta\gamma}$ defined in relation (15) as follows*

$$2G^\alpha = \Gamma^\alpha_{\beta\gamma} y^\beta y^\gamma. \tag{16}$$

Note that this proposition implies the derivatives of $F^2$ are replaced by derivatives of $g_{\alpha\beta}$. Before we prove relation (16) we need two lemmas. The first one concerns the Cartan tensor $C_{\alpha\beta\gamma}(\mathbf{x},\mathbf{y})$ defined as:

$$C_{\alpha\beta\gamma}(\mathbf{x},\mathbf{y}) = \frac{1}{4}\frac{\partial^3 F^2(\mathbf{x},\mathbf{y})}{\partial y^\alpha \partial y^\beta \partial y^\gamma}.$$

**Lemma 1.** *The Cartan tensor $C_{\alpha\beta\gamma}(\mathbf{x},\mathbf{y})$ satisfies*

$$C_{\alpha\beta\gamma}(\mathbf{x},\mathbf{y}) y^\gamma = 0. \tag{17}$$

*Proof.* The Riemann-Finsler metric $g_{\alpha\beta}(\mathbf{x},\mathbf{y})$ inherits the following homogeneity property from the defining property $F(\mathbf{x},\lambda\mathbf{y}) = \lambda F(\mathbf{x},\mathbf{y})$ for all $\lambda \geq 0$:

$$g_{\alpha\beta}(\mathbf{x},\lambda\mathbf{y}) = g_{\alpha\beta}(\mathbf{x},\mathbf{y}).$$

Differentiation with respect to $\lambda$ and setting $\lambda = 1$ yields

$$\frac{\partial g_{\alpha\beta}(\mathbf{x},\mathbf{y})}{\partial y^\gamma} y^\gamma = 0.$$

Consequently, the Cartan tensor satisfies

$$C_{\alpha\beta\gamma}(\mathbf{x},\mathbf{y}) y^\gamma = \frac{1}{2}\frac{\partial g_{\alpha\beta}(\mathbf{x},\mathbf{y})}{\partial y^\gamma} y^\gamma = 0.$$

**Lemma 2.** *The Riemann-Finsler metric tensor satisfies the relations*

$$g_{\alpha\beta} y^\alpha y^\beta = F^2, \tag{18}$$

$$\frac{\partial}{\partial y^\gamma}\left(g_{\alpha\beta} y^\alpha y^\beta\right) = 2 g_{\gamma\alpha} y^\alpha. \tag{19}$$

*Proof.* From the homogeneity of $F$, we can derive the following relations

$$\frac{\partial F}{\partial y^\alpha} y^\alpha = F, \qquad \frac{\partial^2 F}{\partial y^\alpha \partial y^\beta} y^\beta = 0.$$

First we prove relation (18). Using definition (5) we see that

$$\begin{aligned} g_{\alpha\beta} y^\alpha y^\beta &= \frac{1}{2} \frac{\partial}{\partial y^\alpha} \left( \frac{\partial F^2}{\partial y^\beta} \right) y^\alpha y^\beta \\ &= \frac{\partial}{\partial y^\alpha} \left( F \frac{\partial F}{\partial y^\beta} \right) y^\alpha y^\beta \\ &= \left( \frac{\partial F}{\partial y^\alpha} \frac{\partial F}{\partial y^\beta} + F \frac{\partial^2 F}{\partial y^\alpha \partial y^\beta} \right) y^\alpha y^\beta \\ &= \frac{\partial F}{\partial y^\alpha} \frac{\partial F}{\partial y^\beta} y^\alpha y^\beta = F^2, \end{aligned}$$

where we used the relations above. Next, to show (19), we have,

$$\begin{aligned} \frac{\partial}{\partial y^\gamma} \left( g_{\alpha\beta} y^\alpha y^\beta \right) &= \frac{\partial g_{\alpha\beta}}{\partial y^\gamma} y^\alpha y^\beta + g_{\alpha\beta} \delta_{\alpha\gamma} y^\beta + g_{\alpha\beta} y^\alpha \delta_{\beta\gamma} \\ &= 2C_{\alpha\beta\gamma} y^\alpha y^\beta + 2g_{\gamma\beta} y^\beta \end{aligned}$$

using symmetry of $g_{\alpha\beta}$. Furthermore, using Lemma 1, the first term on the right vanishes. □

**Proof of Proposition 1.** Given the lemmas above, the following derivation allows us to rewrite $G^\alpha$ in terms of Christoffel symbols, viz.,

$$\begin{aligned} 2G^\alpha &= \frac{1}{2} g^{\alpha\beta} \left( \frac{\partial}{\partial x^\gamma} \frac{\partial F^2}{\partial y^\beta} y^\gamma - \frac{\partial F^2}{\partial x^\beta} \right) \\ &= \frac{1}{2} g^{\alpha\beta} \left( \frac{\partial}{\partial x^\gamma} \frac{\partial}{\partial y^\beta} (g_{\lambda\mu} y^\lambda y^\mu) y^\gamma - \frac{\partial g_{\lambda\mu}}{\partial x^\beta} y^\lambda y^\mu \right), \end{aligned}$$

where we substituted expression (18) for $F^2$. Next combining this relation with (19), we obtain

$$\begin{aligned} 2G^\alpha(\mathbf{x}, \mathbf{y}) &= \frac{1}{2} g^{\alpha\beta} \left( \frac{\partial}{\partial x^\gamma} (2g_{\beta\lambda} y^\lambda) y^\gamma - \frac{\partial g_{\lambda\mu}}{\partial x^\beta} y^\lambda y^\mu \right) \\ &= \frac{1}{2} g^{\alpha\beta} \left( \frac{\partial g_{\lambda\beta}}{\partial x^\mu} + \frac{\partial g_{\mu\beta}}{\partial x^\lambda} - \frac{\partial g_{\lambda\mu}}{\partial x^\beta} \right) y^\lambda y^\mu \\ &= \Gamma^\alpha_{\lambda\mu} y^\lambda y^\mu, \end{aligned}$$

which completes the derivation of (16). □

Finally, substituting (16) in (13) gives

$$\ddot{x}^\alpha + \Gamma^\alpha_{\beta\gamma} \dot{x}^\beta \dot{x}^\gamma = 0, \tag{20}$$

which is the desired alternative form of the geodesic equations.

## 4 Numerical Model

In order to develop a numerical model, we will focus on a specific HARDI model. We have chosen the fourth-order tensor representation of the Orientation Distribution Function (ODF) [1, 11, 12, 28]. From the DWI data, we compute the ODF as was introduced by Tristán-Vega et al. [28]. In the original literature, the ODF is represented by spherical harmonics. A change of basis allows us to transform the spherical harmonics representation of the ODF to higher order tensor representation. To compute the Finsler metric, we need to compute the spherical inversion of the ODF at each voxel. To achieve this, we apply relation (3) for $m > 15$ different orientations $\mathbf{y}$ on the unit sphere, giving rise to an over-determined system $Y\tilde{\mathbf{d}} = \mathbf{b}$, where $\tilde{\mathbf{d}}$ contains the coefficients; see Table 1. To evenly sample the orientations $\mathbf{y}$ on the sphere, we apply the icosahedron tessellation on the unit sphere. In this chapter, we restrict ourselves to the normalized ODF, hence $\overline{P}_4(\mathbf{x}, \mathbf{y}) = 1$. To compute the solution of this system, least-squares fitting is applied. We rewrite (3) in the form of normal equation $Y^{\mathrm{T}}Y\tilde{\mathbf{d}} = Y^{\mathrm{T}}\mathbf{b}$ where

$$Y = \begin{pmatrix} y_1^1 y_1^1 y_1^1 y_1^1 & \cdots & y_1^3 y_1^3 y_1^3 y_1^3 \\ y_2^1 y_2^1 y_2^1 y_2^1 & \cdots & \cdots \\ \vdots & \vdots & \vdots \\ y_m^1 y_m^1 y_m^1 y_m^1 & \cdots & y_m^3 y_m^3 y_m^3 y_m^3 \end{pmatrix}, \quad \mathbf{b} = \begin{pmatrix} P_4(\mathbf{x}, \mathbf{y}_1)^{-1} \\ \vdots \\ P_4(\mathbf{x}, \mathbf{y}_m)^{-1} \end{pmatrix}. \tag{21}$$

Note that the lower indices of $\mathbf{y}$ indicate the choice of direction and $m$ is the number of gradient directions to sample the ODF profile; in our computations we use $m = 72$. The solution $\tilde{\mathbf{d}}$ is computed using Cholesky factorization. This gives 15 coefficients for the inverted ODF profile. We can fit the new profile over the sphere using the new coefficients $\tilde{\mathbf{d}}$; see Figs. 3 and 4.

Let us introduce $u^\gamma(t) := \dot{x^\gamma}(t)$ for $\gamma = 1, 2, 3$, then we can rewrite system (20) as follows

$$\begin{aligned} \dot{x}^\alpha &= u^\alpha, \\ \dot{u}^\alpha &= -\Gamma^\alpha_{\beta\gamma} u^\beta u^\gamma, \end{aligned} \tag{22}$$

with the $\Gamma^\alpha_{\beta\gamma}$ defined in (15). To solve the system of equations (22) we follow a similar algorithm proposed by Sepasian et al. [24] for the Riemannian metric. Consider $\big(x^1(0), x^2(0), x^3(0)\big)$ a point as the given initial location in the domain and $\big(u^1(0), u^2(0), u^3(0)\big)$ as the initial direction. We compute the solution to (22) for the given initial position and multiple directions using sophisticated ODE solvers such as the fourth order explicit Runge-Kutta method. This gives us a set of geodesics connecting the given initial point to a set of points on the boundary.

The computational domain is discretized uniformly with grid size $h$ and grid points $\mathbf{x}_{ijk} = (x_i^1, x_j^2, x_k^3) = h(i, j, k)$ for $i = 0, 2, 3, \ldots, N - 1$, where $N$ is number of grid points in each spatial direction. For simplicity we take the

**Table 1** Ordering of higher order tensor coefficients

| Tensor element | Coeff. of HOT | Tensor element | Coeff. of HOT |
|---|---|---|---|
| 1 | $D_{1111}$ | 8 | $D_{1223}$ |
| 2 | $D_{1112}$ | 9 | $D_{1233}$ |
| 3 | $D_{1113}$ | 10 | $D_{1333}$ |
| 4 | $D_{1122}$ | 11 | $D_{2222}$ |
| 5 | $D_{1123}$ | 12 | $D_{2223}$ |
| 6 | $D_{1133}$ | 13 | $D_{2233}$ |
| 7 | $D_{1222}$ | 14 | $D_{2333}$ |
|  |  | 15 | $D_{3333}$ |

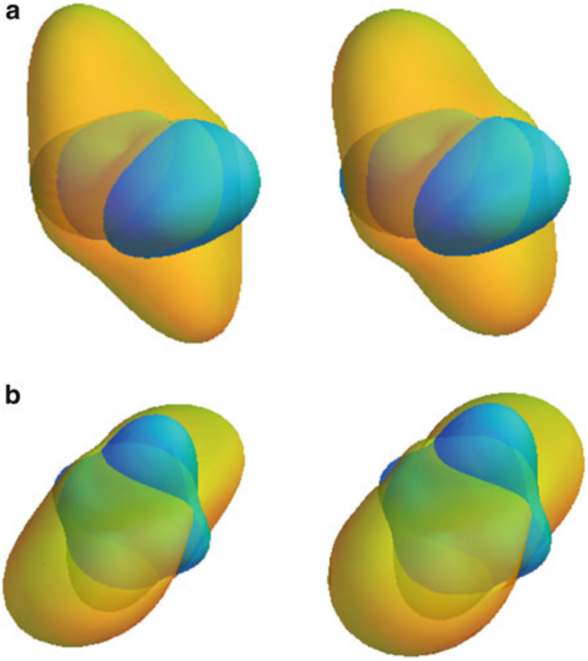

**Fig. 3** ODF (*Blue*) and its inverse (*Yellow*) using least-squares fit (*Left*) and analytic inversion (*Right*). (**a**) ODF and its inverse for a single fiber profile. (**b**) ODF and its inverse for a crossing fiber profile

number of grid points equal in all directions. For each grid point, we assign the 15 coefficients of inverted HOT $\tilde{\mathbf{D}}$ (see Fig. 5 top).

We approximate the derivatives of $g_{\alpha\beta}(\mathbf{x},\mathbf{y})$ at each grid point by the standard second order central difference scheme, for example,

$$\frac{\partial g_{\alpha\beta}}{\partial x^1}(x_i^1, x_j^2, x_k^3, \mathbf{y}) \approx \frac{1}{2h}\left(g_{\alpha\beta}(x_{i+1}^1, x_j^2, x_k^3, \mathbf{y}) - g_{\alpha\beta}(x_{i-1}^1, x_j^2, x_k^3, \mathbf{y})\right). \quad (23)$$

Second order one-sided differences are applied when the grid points are situated on the boundary, e.g,

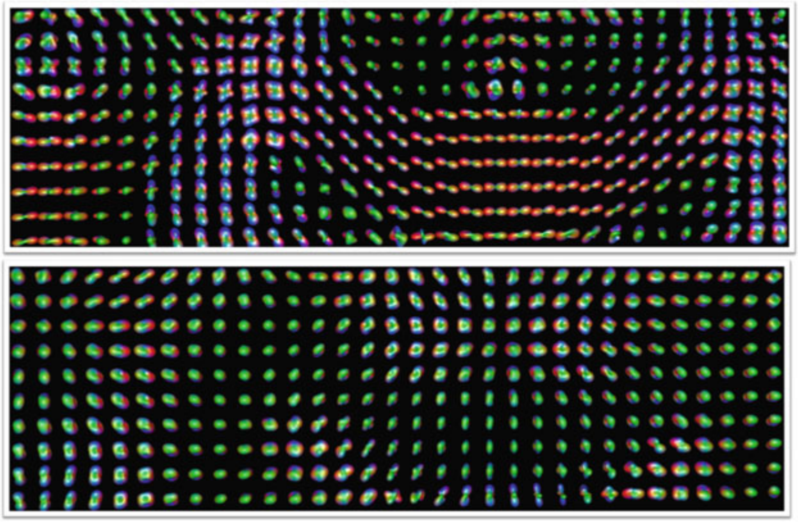

**Fig. 4** Fourth order ODF field (*top image*) and its inverted field (*bottom image*) from part of the centrum semiovale

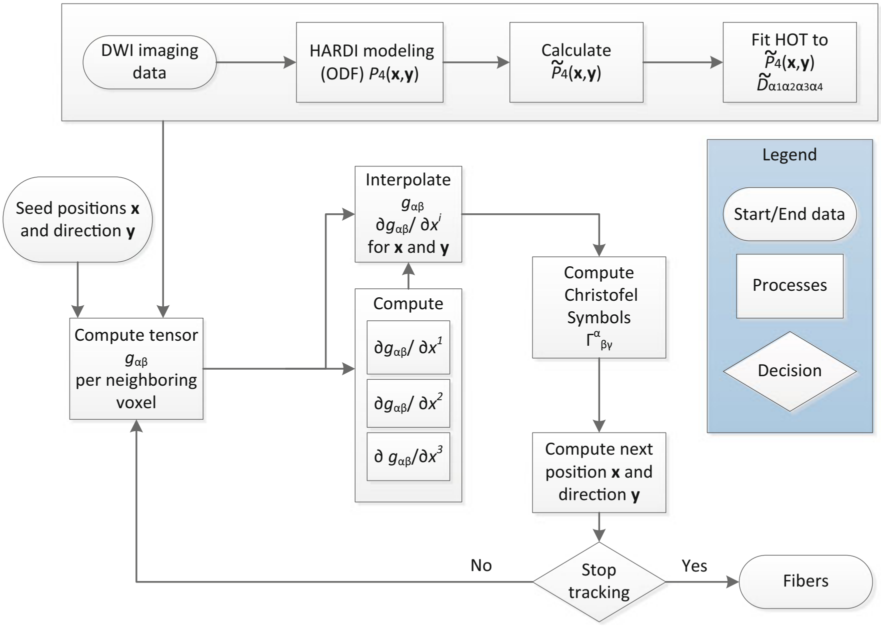

**Fig. 5** Flowchart for the ray tracing algorithm to reconstruct geodesics in a Finsler space

$$\frac{\partial g_{\alpha\beta}}{\partial x^1}(x_0^1, x_j^2, x_k^3, \mathbf{y}) \approx$$
$$\frac{1}{2h}\left(-3g_{\alpha\beta}(x_0^1, x_j^2, x_k^3, \mathbf{y}) + 4g_{\alpha\beta}(x_1^1, x_j^2, x_k^3, \mathbf{y}) - g_{\alpha\beta}(x_2^1, x_j^2, x_k^3, \mathbf{y})\right). \qquad (24)$$

Note that similar expressions hold for derivatives with respect to $x^2$ and $x^3$. Note the dependence of these relations on the argument $\mathbf{y}$. Solving the ODE system gives the solution at points that are not necessarily located in the grid points. Therefore, the value of the metric and its derivatives are not defined there, and we apply trilinear interpolation at any point in the domain where the value of the metric is not available. Initial vectors are uniformly distributed over the unit sphere using the vertices of regular symmetrical polyhedra. The integration of geodesics continues till they hit the boundary of the computational domain. Once all geodesics are computed for the initial seed points and given initial directions, one can select the fibers by selecting the regions of interests and filter all geodesics that pass through both selected regions. Geodesics are computed until they meet one of the boundaries, therefore to determine the fiber connecting two given regions we apply the line-plane intersection. This allows us to cut off the geodesics once they enter one of the selected regions. The flow chart in Fig. 5 summarizes the ray-tracing tractography algorithm for HARDI. The algorithm has the following stages:

1. Compute the coefficients of the inverted ODFs using the least-squares fit as described in this section (see Fig. 5 top).
2. Fetch an initial seed point and direction, which becomes the current position and direction.
3. Find the eight neighboring voxels forming the cell of the current position and compute for each neighboring voxel the metric tensor according to Eq. (7).
4. Compute the derivatives at the neighboring voxels.
5. Compute the metric tensor and its derivatives at the current position using trilinear interpolation.
6. Compute the Christoffel symbols, as defined in Eq. (15).
7. Compute the next position and direction of the fiber, from (22)
8. Repeat step 3–6 until the stopping criterion (i.e., meeting the domain boundaries) is fulfilled.

## 5 Results

In this section we present the first results we have obtained with the ray-tracing tractography algorithm described in this chapter. We generated synthetic tensor fields simulating two fiber bundles crossing at angles 90° and 60°. To generate the tensors in the crossing area the Gaussian mixture model introduced by Tuch et al. [29] has been used. The signal is obtained simulating a $b$-value of 1,000 s/mm$^2$ and voxel resolution $1 \times 1 \times 1$ mm. Riccian noise with $SNR = 15$ is added to the images.

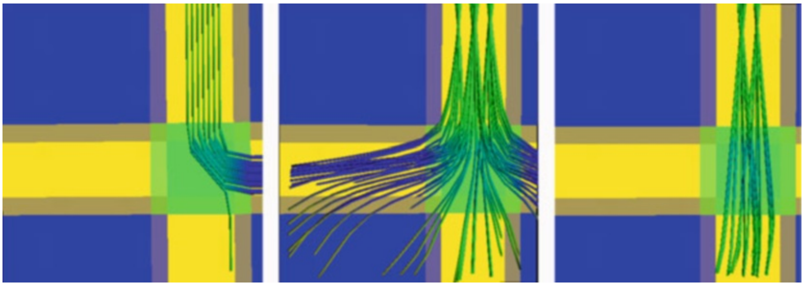

**Fig. 6** 90° crossing. From left to right: streamline tractography for DTI, geodesic ray tracing for DTI, geodesic ray tracing for HARDI

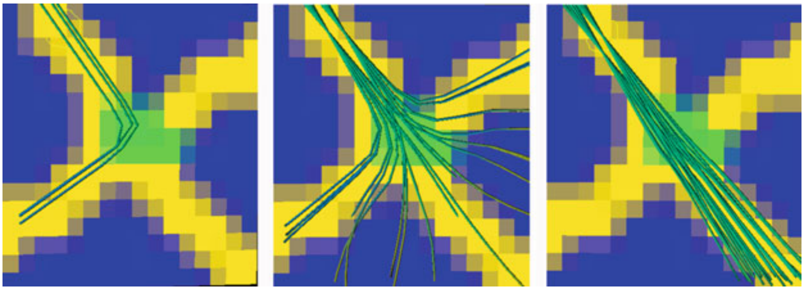

**Fig. 7** Rotated 90° crossing. From left to right: streamline tractography for DTI, geodesic ray tracing for DTI, HARDI multi-valued geodesic

Results for the 90° crossing angle are shown in Fig. 6. The behavior of the streamline (left), DTI ray-tracing [25] (middle) and HARDI ray-tracing (right) tractography are illustrated. The results illustrate that streamlines have a preference for curving instead of going straight. The HARDI ray-tracing tractography gives less spreading of the reconstructed fiber bundles compared to the DTI ray-tracing method. Figure 7 shows the behavior of these algorithms with respect to rotation. The crossing angle here remains 90° and the data is rotated 55°. Figure 8 illustrate fiber bundles for the 60° crossing angle. We see that for a sharper angle the algorithm is still capable of capturing crossing fibers.

In order to provide preliminary results of HARDI ray-tracing tractography for real data, Fig. 9 shows the tractography result using a $10 \times 10 \times 30$ cube cut from the human data set obtained by a Philips scanner with resolution $2 \times 2 \times 2$ mm, $b$-value of 1,000 s/mm$^2$ and 128 gradient directions. The fiber tracking stops in both cases if the fibers meet one of the boundaries. These preliminary results show the capability of the tractography algorithm for capturing realistic fiber tracts in the area of corona radiata (CR), corpus callosum (CC) and cingulum (CG). However, these are preliminary results and future research and experiments are needed to fully explore the capabilities of the presented method.

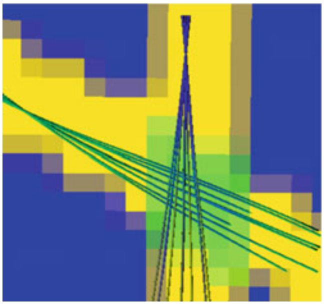

**Fig. 8** Geodesic ray tracing for HARDI using 60° crossing

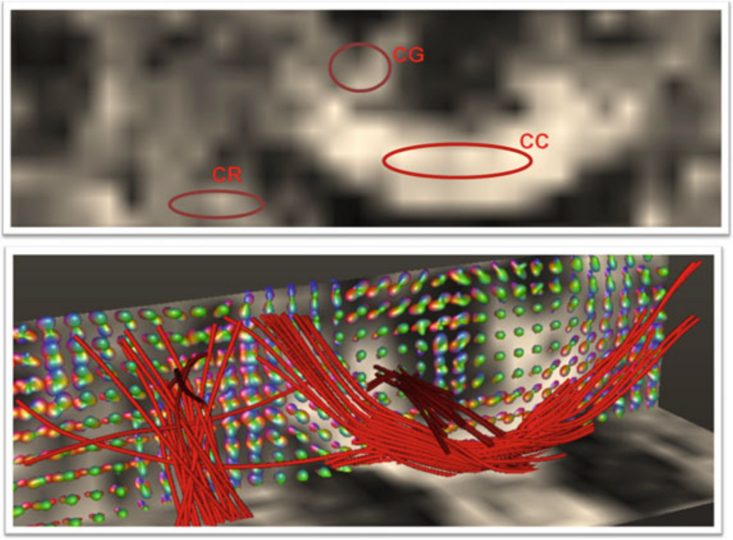

**Fig. 9** Tractography results in the crossing region of Fig. 4. The *top image* indicates the seed regions in a fractional anisotropy map, the *bottom image* shows the ray-tracing tractography results for CC, CR and CG

## 6 Conclusion

In this chapter, we presented a new tractography algorithm for HARDI data. Our method is based on computing geodesics in the Finsler metric as an extension of Riemannian metric. The Finsler metric is defined as function of position and direction using HARDI data at each voxel. We made a heuristic choice concerning the mapping of the HARDI data into a Finsler metric. For future work, it would be interesting to study other possibilities. Compared to other existing geodesic based HARDI tractography methods, we computed multi-valued solutions of geodesic equations instead of single valued viscosity solutions. We presented the theory and showed the potential of our method for capturing crossing fibers. Results of synthetic data and very preliminary human brain data results showed the applicability of the method. These are encouraging results that need further experimentation to explore its possibilities and compare it to other existing fiber tracking methods.

## References

1. Aganj, I., Lenglet, C., Sapiro, G.: ODF reconstruction in q-ball imaging with solid angle consideration. In: The 6th IEEE International Symposium on Biomedical Imaging (ISBI), Boston, pp. 1398–1401 (2009)
2. Alexander, D.C., Barker, G., Arridge, S.: Detection and modeling of non-Gaussian apparent diffusion coefficient profiles in human brain data. Magn. Reson. Med. **48**(2), 331–340 (2002)
3. Astola, L., Florack, L.: Finsler geometry on higher order tensor fields and applications to high angular resolution diffusion imaging. Int. J. Comput. Vis. **92**, 325–336 (2011)
4. Basser, P.J., Pierpaoli, C.: Microstructural and physiological features of tissues elucidated by quantitative-diffusion-tensor MRI. J. Magn. Reson. **111**(1), 209–219 (1996)
5. Behrens, T.E.J., Berg, H.J., Jbabdi, S., Rushworth, M.F.S., Woolrich, M.W.: Probabilistic diffusion tractography with multiple fibre orientations: what can we gain? NeuroImage **34**(1), 144–155 (2007)
6. Blair, D.E.: Inversion Theory and Conformal Mapping. American Mathematical Society, Providence (2000)
7. Lenglet, C., Deriche, R., Faugeras, O.D.: Inferring white matter geometry from diffusion tensor MRI: application to connectivity mapping. In: Proceedings of 8th European Conference on Computer Vision, Prague, pp. 127–140 (2004)
8. Campbell, J.S.: Diffusion imaging of white matter fibre tracts. PhD thesis, McGill University, Montreal (2004)
9. Chern, S., Shen, Z.: Lectures on Finsler geometry. Nankai Tracts Math. **6** (2003)
10. Morris, D.M., Embleton, K.V., Parker, G.J.: Probabilistic fibre tracking: differentiation of connections from chance events. NeuroImage **42**(4), 1329–1339 (2008)
11. Descoteaux, M.: High angular resolution diffusion MRI: from local estimation to segmentation and tractography. Ph.D. Thesis, Universite de Nice, Sophia Antipolis (2008)
12. Descoteaux, M., Angelino, E., Fitzgibbons, S., Deriche, R.: Regularized, fast and robust analytical q-ball imaging. Magn. Reson. Med. **58**(3) (2007)
13. Descoteaux, M., Deriche, R., Knoesche, T., Anwander, A.: Deterministic and probabilistic tractography based on complex fiber orientation distributions. IEEE Trans. Med. Imaging **2**(28), 269–286 (2008)
14. Donnell, L.O., Haker, S., Westin, C.F.: New approaches to estimation of white matter connectivity in diffusion tensor MRI: Elliptic PDEs and geodesics in a tensor-warped space. In: International Conference on Medical Image Computing and Computer-Assisted Intervention – MICCAI'02, Tokyo, vol. 2488, pp. 459–466 (2002)
15. Hagmann, P., Reese, T., Tseng, W., Meuli, R., Thiran, J., Wedeen, V.: Diffusion spectrum imaging tractography in complex cerebral white matter: an investigation of the centrum semiovale. In: ISMRM, Kyoto, vol. 12. International Society for Magnetic Resonance in Medicine (2004)
16. Lenglet, C., Prados, E., Pons, J.P., Deriche, R., Faugeras, O.: Brain connectivity mapping using Riemannian geometry, control theory and PDEs. SIAM J. Imaging Sci. (SIIMS) **2**(2), 285–322 (2009)
17. Melonakos, J., Pichon, E., Angenent, S., Tannenbaum, A.: Finsler active contours. IEEE Trans. Pattern Anal. Mach. Intell. **30**(3), 412–423 (2008)

18. Mo, X.: An Introduction to Finsler Geometry. Volume 1 of Peking University Series in Mathematics. World Scientific, Singapore (2006)
19. Ozarslan, E., Shepherd, T., Vemuri, B., Blackband, S., Mareci, T.: A nonparametric reconstruction and its matrix implementation for the diffusion orientation transform (dot). In: The 3rd IEEE International Symposium on Biomedical Imaging: Nano to Macro (ISBI), Arlington, pp. 85–88 (2006)
20. Parker, G.J.M., Alexander, D.C.: Probabilistic anatomical connectivity derived from the microscopic persistent angular structure of cerebral tissue. Philos. Trans. R. Soc. Lond. B: Biol. Sci. **360**(1457), 893–902 (2005)
21. Péchaud, M., Descoteaux, M., Keriven, R.: Brain connectivity using geodesics in HARDI. In: International Conference on Medical Image Computing and Computer-Assisted Intervention – MICCAI'09, London, pp. 482–489 (2009)
22. Pichon, E., Westin, C., Tannenbaum, A.: A Hamilton-Jacobi-Bellman approach to high angular resolution diffusion tractography. In: International Conference on Medical Image Computing and Computer-Assisted Intervention – MICCAI'05, Palm Springs. Lecture Notes in Computer Science, pp. 180–187 (2005)
23. Rund, H.: The Hamilton-Jacobi Theory in the Calculus of Variations. Robert E. Krieger Publishing, Huntington (1973)
24. Sepasian, N., ten Thije Boonkkamp, J., ter Haar Romeny, B., Vilanova, A.: Multivalued geodesic ray-tracing for computing brain connections using diffusion tensor imaging. SIAM J. Imaging Sci. **5**(2), 483–504 (2012)
25. Sepasian, N., ten Thije Boonkkamp, J., Vilanova, A., ter Haar Romeny, B.: Multi-valued geodesic based fiber tracking for diffusion tensor imaging. In: MICCAI'09, Diffusion Modeling and the Fiber Cup Workshop, London, vol. 1, pp. 6–13 (2009)
26. Shen, Z.: Lectures on Finsler Geometry. World Scientific, Singapore (2001)
27. Tournier, J.D., Calamante, F., Connelly, A.: Robust determination of the fibre orientation distribution in diffusion mri: non-negativity constrained super-resolved spherical deconvolution. NeuroImage **35**(4), 1459–1472 (2007)
28. Tristán-Vega, A., Westin, C.F., Aja-Fernández, S.: Estimation of fiber orientation probability density functions in high angular resolution diffusion imaging. NeuroImage **47**(2), 638–650 (2009)
29. Tuch, D., Reese, T., Wiegell, M., Makris, N., Belliveau, J.W., Wedeen, V.: High angular resolution diffusion imaging reveals intravoxel white matter fiber heterogeneity. Magn. Reson. Med. **48**, 577–582 (2002)
30. Tuch, D.S.: Q-ball imaging. Magn. Reson. Med. **52**(6), 1358–1372 (2004)
31. Wedeen, V.J., Hagmann, P., Tseng, W.Y.I., Reese, T.G., Weisskoff, R.M.: Mapping complex tissue architecture with diffusion spectrum magnetic resonance imaging. Magn. Reson. Med. **54**(6), 1377–1386 (2005)